International Journal of Engineering Inventions
e-ISSN: 2278-7461, p-ISSN: 2319-6491
Volume 14, Issue 12 [December 2025] PP: 83-92

Efficient Photoremoval of Manganese (Mn^{+2}) from Aqueous Solutions Using a CdSe/CdTe Nanocomposite

Sevil AKÇAĞLAR
Department of Mechanical Engineering, Faculty of Engineering, Dokuz Eylül University, İzmir, Turkey,
Corresponding Author: sevil.akcaglar@deu.edu.tr

ABSTRACT: *The increasing contamination of water sources with uranium (Mn^{+2}) poses a serious threat to environmental and human health. In this work, a CdSe/CdTe nanocomposite was synthesized via a facile two-step hydrothermal method and employed as a visible-light-responsive photocatalyst for the efficient removal of (Mn^{+2}) from aqueous solutions. The CdSe/CdTe heterojunction effectively enhances charge separation through the formation of an internal electric field, significantly improving the photocatalytic reduction of (Mn^{+2}) to less soluble uranium species. Under simulated solar light irradiation, up to 92 % of (Mn^{+2}) (C_0 = 30 mg L^{-1}) was removed within 5 minutes without the need for sacrificial agents or inert gas protection. The photocatalyst exhibited excellent stability and reusability, maintaining its high efficiency even in the presence of competing ions. The synergistic interaction between CdSe and CdTe, combined with the intrinsic role of Te^{2-} as a hole scavenger, was found to be critical in enhancing the reduction kinetics. Benefiting from this synergistic effect, the (Mn^{+2}) removal rate can be optimized to as high as 14.4 mmol g^{-1} h^{-1}. This study demonstrates the potential of CdSe/CdTe nanocomposites as highly efficient, solar-driven materials for the photoremoval of (Mn^{+2}), offering a sustainable approach to radioactive wastewater treatment.*

Keywords: *Manganese (Mn^{+2}) removal, CdSe/CdTe nanocomposite, Photocatalysis, Solar light, Heterojunction, Radioactive wastewater, Charge separation, Environmental remediation*

Date of Submission: 12-12-2025 Date of acceptance: 24-12-2025

I. INTRODUCTION

In the face of global climate change, achieving carbon neutrality by 2050 stands as one of the most critical goals for modern civilization. Attaining this target requires a substantial reduction in the dependence on fossil fuels and a comprehensive optimization of the current energy structure. Among the available carbon-free energy sources, nuclear power has attracted growing attention due to its high energy density and stable output [1]. Nevertheless, the increasing demand for uranium (U)—an indispensable nuclear fuel—has simultaneously intensified concerns regarding its severe radiotoxicity to living organisms and ecosystems [2, 3]. Beyond the potential challenges related to uranium supply security, the environmental consequences of uranium exploitation and utilization have become a major issue [4]. In particular, uranium-containing wastewater produced during mining, ore refining, and nuclear power plant operations represents a serious environmental hazard and a threat to human health [2], [5-7].

In nature, uranium (U) commonly exists in two oxidation states: hexavalent (Mn^{+2}) and tetravalent (Mn^{+2}) [8]. Among these, (Mn^{+2})is of particular concern because it typically occurs as the water-soluble uranyl ion (UO_2^{2+}), which is primarily responsible for the biotoxicity of uranium [9]. In biological systems, (Mn^{+2}) can severely disrupt photosynthesis in plants [7], induce DNA damage in animal cells [3], and impair the human nervous system [2]. Therefore, developing efficient and environmentally friendly strategies for its removal remains one of the key research priorities in the field.

Over the past few decades, photocatalysis has been extensively employed for the degradation of heavy metals and organic pollutants [10–12]. The mechanism involves the excitation of electrons from the valence band to the conduction band of a photocatalyst under light irradiation, leading to a series of redox reactions [13–17]. As a result, pollutants are transformed into less toxic or harmless substances through photochemical reactions [18]. Compared with conventional approaches such as adsorption, ion exchange, and membrane separation, photocatalysis stands out for its simplicity, high efficiency, low cost, and excellent reusability [19–22]. In particular, the photocatalytic reduction of (Mn^{+2}) to the water-insoluble (Mn^{+2}) species provides a promising and practical approach that simultaneously enables uranium recovery and environmental remediation [23–26].

Existing photocatalytic technologies generally involve a homogeneous mixture of photocatalysts with (Mn^{+2})-containing pollutants, where the photoinduced redox process relies heavily on active interfacial reactions. However, this requirement often leads to complex catalyst fabrication procedures and hinders long-

term photocatalytic stability. In recent years, interface engineering of CdX-based composites—where X represents group VI-A elements such as S, Se, and Te—has been extensively explored for the efficient photoremoval of (Mn^{+2}) [27–29]. Compared with conventional photocatalysts, these interface-engineered CdX-based materials offer significant advantages, including abundant interfacial sites, enhanced light-harvesting capability, and tunable energy-level structures.

For instance, pure CdS suffers from limited active sites and rapid recombination of photogenerated electron–hole pairs, whereas CdSe tends to exhibit overly stable adsorption that restricts reaction dynamics. To address these drawbacks, ternary [30], and binary [31] CdX-based composites have attracted considerable interest due to their ability to balance adsorption behavior and photoinduced redox activity while facilitating efficient charge separation. The hybridization of advanced photocatalysts with CdX has been shown to further enhance overall performance. Mechanistically, n-type CdX semiconductors can generate an internal electric field directed toward other components at the heterointerface, thereby promoting charge transfer from CdX to adjacent phases. Moreover, the distinct interfaces between materials with different band gaps facilitate synergistic mass transfer and accelerate electron conduction.

Despite these promising attributes, the synthesis and operation of many CdX-based composites often involve stringent conditions or complicated procedures, which limit their large-scale or practical application.

In this work, a simple two-step hydrothermal method was employed for the interfacial and elemental engineering of a novel CdSe/CdTe heterojunction. The physicochemical properties and photocatalytic behavior of the resulting composite were systematically investigated. Under simulated sunlight, an impressive (Mn^{+2}) removal efficiency of up to 92 % was achieved within just five minutes, corresponding to a maximum removal rate of 14.4 mmol · g^{-1} · h^{-1}. Remarkably, this high removal efficiency was well maintained under real sunlight and in the presence of various coexisting ions. Furthermore, the photocatalyst exhibited excellent stability and recyclability, retaining 71 % of its initial removal efficiency even after four consecutive cycles.

The underlying mechanism responsible for this outstanding performance was further explored. Results revealed that the built-in electric field generated within the CdSe/CdTe heterojunction was significantly stronger than that in pristine CdSe or CdTe, effectively enhancing charge separation and transfer. In addition, the presence of Te^{2-} species acted synergistically as an intrinsic hole-trapping center and a hydroxyl radical sacrificial agent, collectively contributing to the superior photocatalytic reduction of (Mn^{+2}).

II MATERIALS AND METHODS

2.1. Chemicals and Reagents

Ethylenediamine, uranyl nitrate hexahydrate, sodium hydroxide, nitric acid, chloroacetic acid, sodium acetate, Arsenazo III ($C_{22}H_{18}(As_2)N_4O_{14}S_2$), sodium tellurite ($Na_2TeO_3$), polyvinylpyrrolidone (PVP, K90, Mw ≈ 130,000), ammonia, hydrazine hydrate ($N_2H_4·H_2O$), acetone, selenium powder (Se, 200 mesh), cadmium nitrate tetrahydrate ($Cd(NO_3)_2·4\,H_2O$), potassium bicarbonate ($KHCO_3$), sodium oxalate, disodium ethylenediaminetetraacetate (EDTA-2Na), ammonium oxalate, methanol, isopropanol, silver nitrate ($AgNO_3$), 4-benzoquinone, polyvinylidene fluoride (PVDF), N,N-dimethylformamide (DMF), and anhydrous ethanol were used in this study. All chemicals were of analytical grade and purchased from commercial suppliers without further purification. Ultrapure water (∼18 MΩ·cm) prepared in the laboratory was used for solution preparation and washing procedure

2.2. Synthesis of Tellurium Nanotubes (Te NTs)

Te NTs were synthesized via a modified hydrothermal method based on a previously reported procedure [32]. Briefly, 1.5 g of polyvinylpyrrolidone (PVP) and 138.0 mg of Na_2TeO_3 were dissolved in 37.5 mL of ultrapure water and stirred at room temperature for 30 min. Subsequently, 15.0 mL of acetone, 5.0 mL of ammonia, and 2.5 mL of hydrazine hydrate ($N_2H_4·H_2O$) were added, and the mixture was stirred for an additional 30 min. After cooling to room temperature, the solution was transferred to a 100 mL Teflon-lined stainless-steel autoclave and heated at 180 °C for 4 h. The resulting product was then allowed to cool naturally, followed by sequential washing with ultrapure water and ethanol, and finally dried under vacuum at 60 °C to obtain the Te NTs.

2.3. Synthesis of $CdSe_xTe$ (CST-X)

$CdSe_xTe$ (CST-X) nanocomposites were prepared via a modified hydrothermal method [33,34]. Briefly, 0.5 mmol of $Cd(NO_3)_2·4\,H_2O$ was dissolved in 15 mL of ethylenediamine (EDA) under vigorous stirring to form a homogeneous solution. A mixture of Se powder and Te NTs (total 0.5 mmol) with the desired Se:Te molar ratio was then added, followed by 1.5 mL of hydrazine hydrate ($N_2H_4·H_2O$) and stirring for 30 min. The solution was transferred to a 50 mL Teflon-lined autoclave and heated at 140 °C for 12 h. After cooling to room temperature, the product was centrifuged at 8000 rpm for 3 min, washed repeatedly with ethanol, and dried under vacuum at 60 °C.

Se: Te ratios were investigated: 0, 0.2, 0.4, 0.5, 0.6, 0.8, 0.9, and 1, corresponding to CdTe, $CdSe_{0.2}Te_{0.8}$, $CdSe_{0.4}Te_{0.6}$, $CdSe_{0.5}Te_{0.5}$, $CdSe_{0.6}Te_{0.4}$, $CdSe_{0.8}Te_{0.2}$, $CdSe_{0.9}Te_{0.1}$, and CdSe, respectively. For simplicity, these samples are denoted as CST-X, where X = 0, 2, 4, 5, 6, 8, 9, and 10.

2.4. Characterization

The morphology and elemental distribution of the samples were examined by transmission electron microscopy (TEM, FEI Talos F200x G2) coupled with energy-dispersive X-ray spectroscopy (EDS). Crystallographic structures were analyzed using X-ray diffraction (XRD, TD5000, Dandong Tongda Technology, China). Surface chemical composition and oxidation states were determined by X-ray photoelectron spectroscopy (XPS, Thermo Fischer ESCALAB Xi+, Al Kα, hν = 1486.7 eV). UV–vis absorption and diffuse reflectance spectra (DRS) were recorded with UV-2910 and UV-3910 spectrophotometers (Shimadzu, Japan).

2.5. Batch Photocatalysis Experiment

For photocatalytic tests, 10 mg of CST-X was dispersed in 100 mL of 30 ppm UO_2^{2+} solution (≈0.13 mM) in a quartz reactor, with pH adjusted using nitric acid or sodium hydroxide. The mixture was stirred in the dark for 120 min to achieve adsorption–desorption equilibrium, followed by 90 min under simulated sunlight (300 W Xe lamp). At specific intervals, 1 mL samples were withdrawn, filtered (0.22 μm cellulose acetate), and analyzed by UV–Vis spectroscopy using Arsenazo III (λ = 652 nm). [30], [35-37].

Control experiments without CST-X were performed for comparison. The anti-interference ability was assessed by pre-mixing 0.5 mM common ions (Na^+, K^+, Ca^{2+}, Mg^{2+}, Al^{3+}, Zn^{2+}, Cu^{2+}, Ni^{2+}, Cr^{3+}, SO_4^{2-}, Cl^-, CO_3^{2-}) with 0.1 mM UO_2^{2+} at pH 5. Recyclability was tested by desorbing adsorbed (Mn^{+2}) with 0.5 M $KHCO_3$ for 5 h, washing with ultrapure water, drying at 60 °C, and reusing in subsequent cycles.

Mechanistic studies were conducted by adding sacrificial agents: $Na_2C_2O_4$, EDTA-2Na, ammonium oxalate, and methanol for holes (h^+), isopropanol for •OH, $AgNO_3$ for electrons (e^-), and 4-benzoquinone for $•O_2^-$ [19], [27].

III RESULTS AND DISCUSSION

Te nanorods were successfully synthesized via the hydrothermal method (Fig. 1) [34,35]. The fabricated CST-8 consists of smooth, hollow rods with lengths of 150–250 nm, decorated with smaller rod-like branches resembling antlers, which enhance pollutant adsorption for photocatalysis (Fig.1a) High-resolution TEM images reveal distinct lattice fringes corresponding to CdSe ((201)/(200)/(101): 0.181/0.187/0.329 nm) and CdTe ((311)/(220): 0.193/0.226 nm) in CST-8 (Fig. 1a) EDS mapping further confirms the uniform distribution of Cd, Se, and Te throughout the structure (Fig. 1bThese results indicate that the two-step hydrothermal method successfully engineered CST-8 with abundant submicron structures and well-defined lattice interfaces.

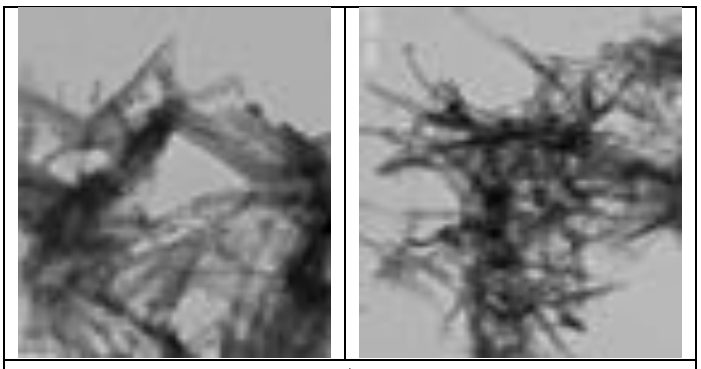

A

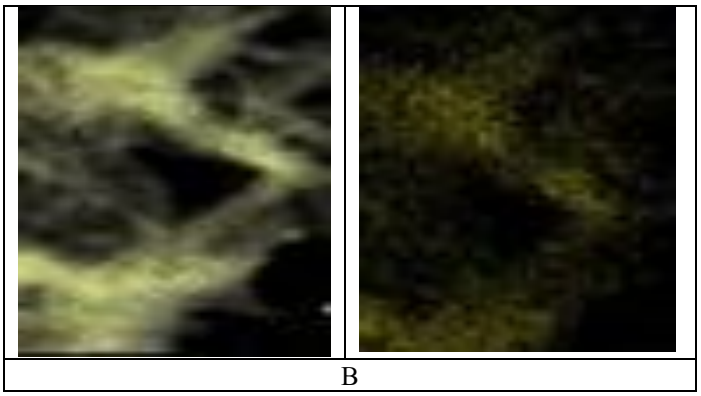

B

Fig. 1. A TEM images of CST-8. B EDS element maps of total

To further probe its structural features, CST samples were analyzed by XRD and UV–Vis spectroscopy. As shown in Fig. 2a, CST-8 exhibits XRD peaks corresponding to CdSe ((100), (002), and (101)) as well as CdTe ((111), (220), and (311)), confirming the presence of multiple CdSe/CdTe heterointerfaces, consistent with TEM observations.. The UV–Vis spectrum of CST-8 (Fig. 2b) demonstrates absorption features of both CdSe and CdTe. [35]. Similarly, the Se 3d (54.2 and 53.5 eV) and Te 3d (582.6 and 572.3 eV) peaks show minimal shifts, confirming that the chemical states of Se and Te remain unchanged regardless of their ratio [40].

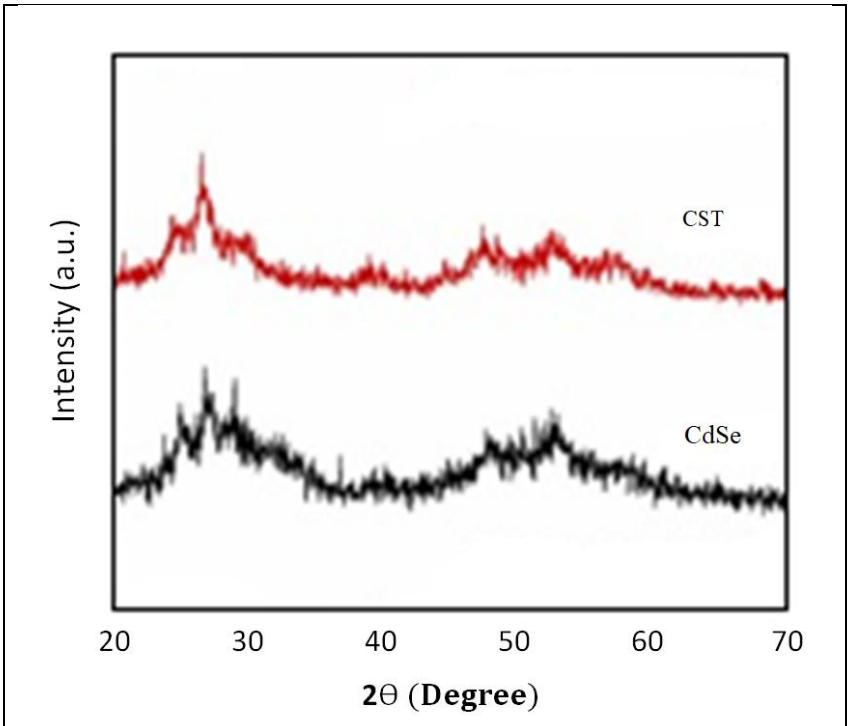

A

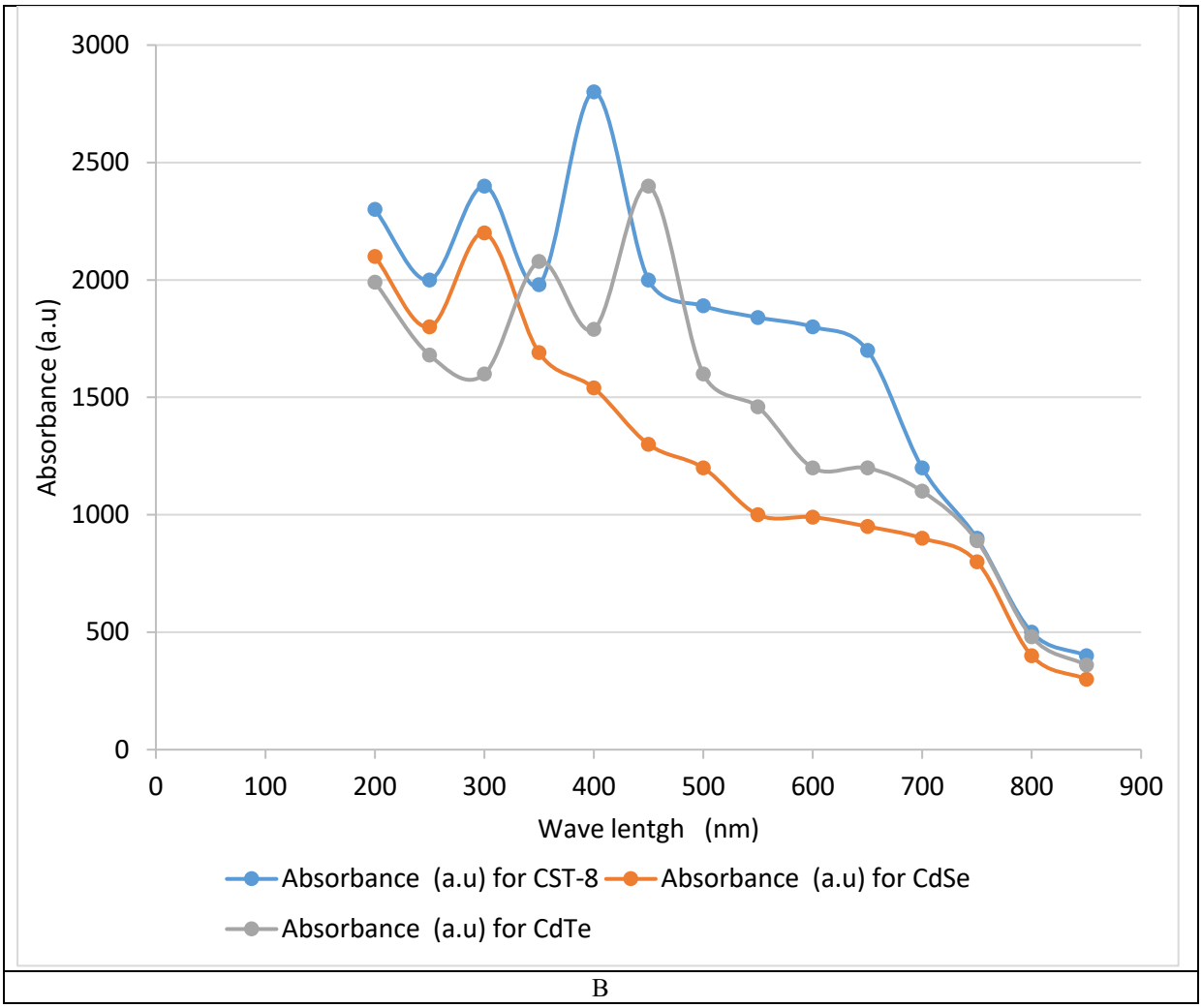

B

Fig. 2. (A) XRD patterns and (B) UV-Vis spectra of CST-8.

pH is a key factor in (Mn^{+2}) removal [40]. As shown in Fig. 3, CST-8 exhibits optimal performance at pH 5. During 120 min dark pre-stirring (Fig. 3), adsorption ranged from 1 % (pH 3) to 56 % (pH 6).

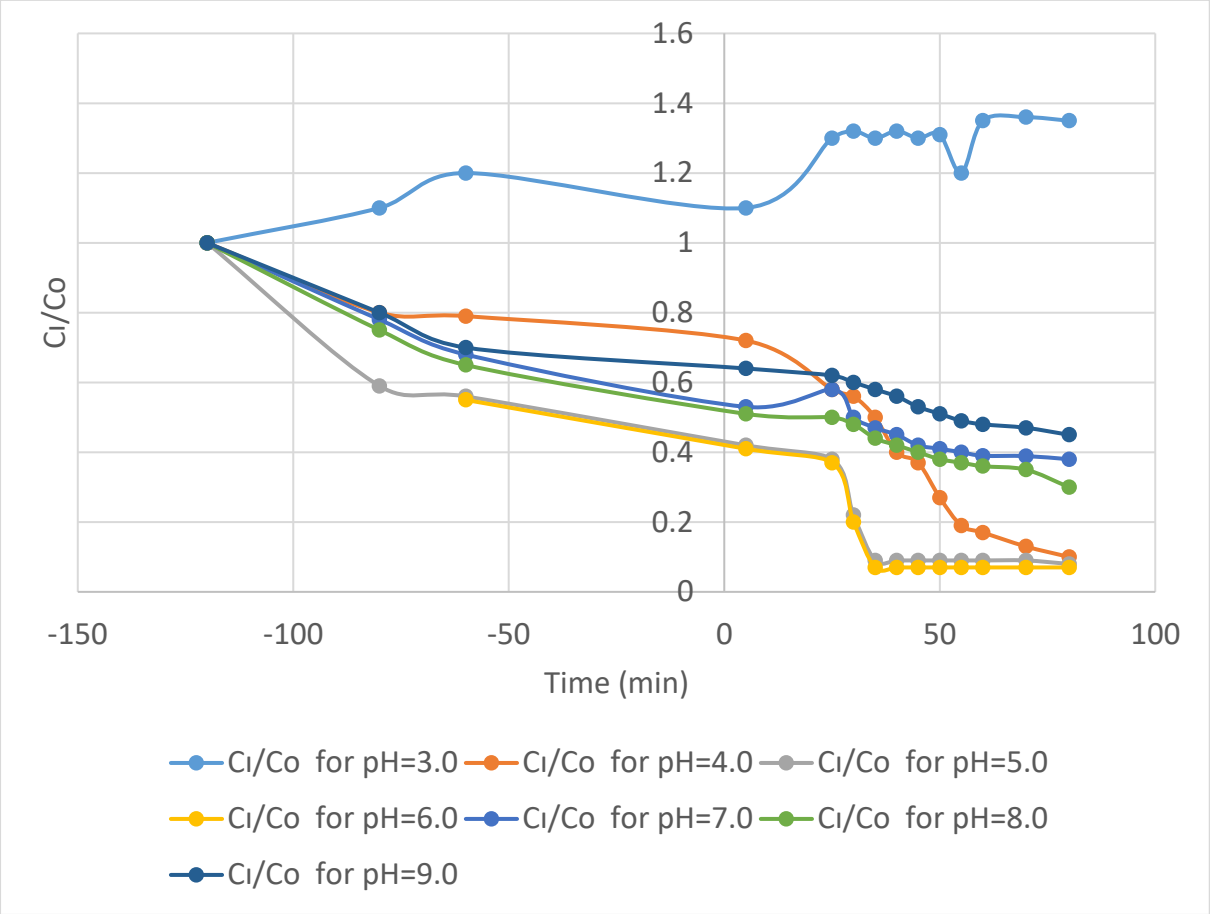

Fig. 3. Effects of pH on the (Mn^{+2}) removal by CST-8 with C_0 = 30 mg/L: time-dependence,

Photocatalyst type significantly affects (Mn^{+2}) removal. During 120 min dark adsorption, pure CdSe adsorbs more than CdTe, while CST-8 shows the least (CdSe > CdTe > CST-8, Fig. 2A). However, under light, CST-8 exhibits the highest rate constant (0.188 min^{-1}) compared to 0.043 for CdTe and 0.023 for CdSe (Fig. 2B), indicating that light-driven photocatalysis, rather than adsorption, dominates (Mn^{+2}) removal on CST-8.

Dark adsorption is minimal for most CST-X except CST-9 (66 %). Upon illumination, (Mn^{+2}) removal and rate constants increase with CdSe content (CST-2 → CST-8, 0.044 → 0.188), while CST-9 resembles CdSe with the lowest rate (0.040). This suggests the enhanced removal arises from synergistic photo-induced reactions at CdSe/CdTe interfaces, explaining the efficiency order: CST-8 > CST-9 > CdSe.

Dosage effects of CST-8 were also investigated (Fig. 4). Increasing CST-8 amount improves (Mn^{+2}) removal under both dark and light, with 10 mg showing slightly better dark adsorption than 8 mg, but similar light-driven performance, indicating that photocatalysis is the main contributor. Rate constant data confirm this trend. Under natural sunlight (~60 mW/cm^2, 90 min, 27–30 °C), CST-8 achieves 96 % (Mn^{+2}) removal demonstrating its practical potential.

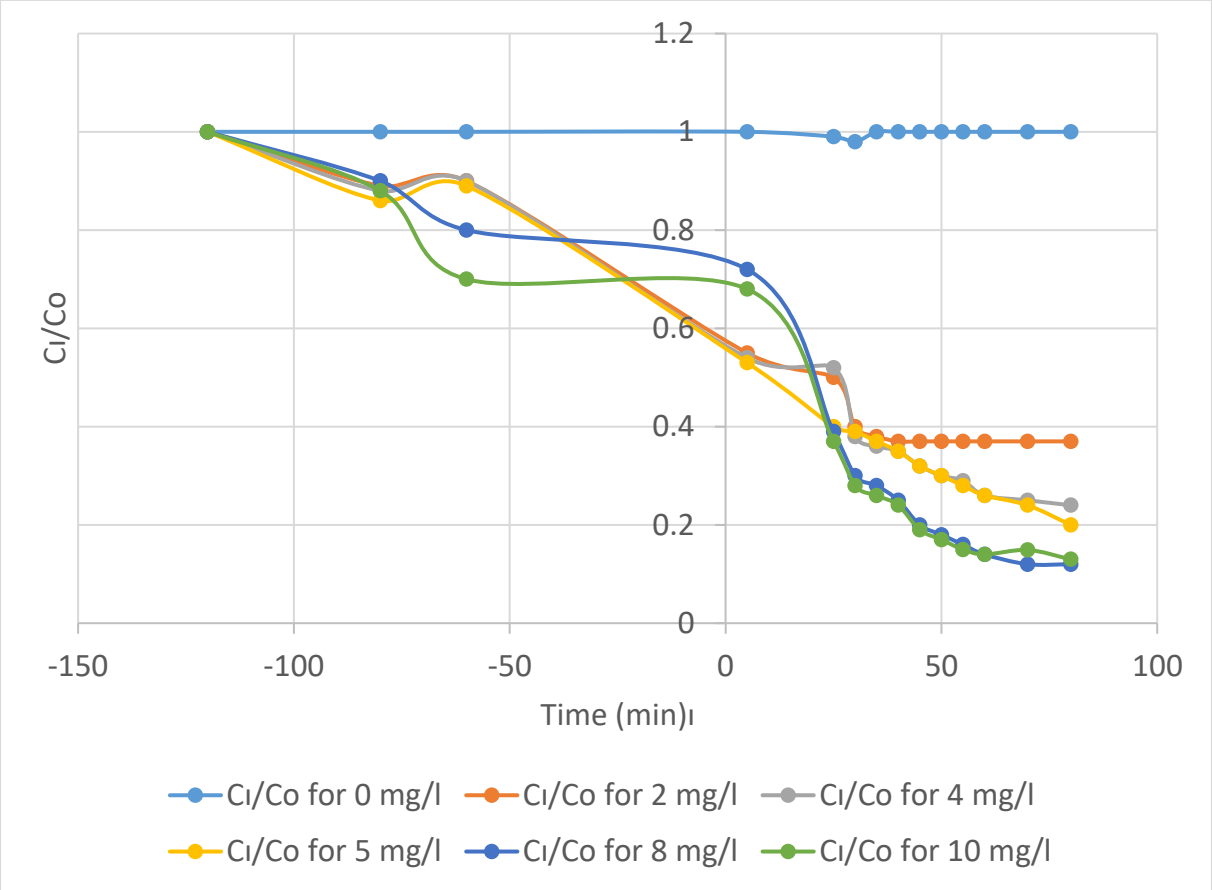

Fig. 4. The photocatalytic performance of CST-8 for the (Mn^{+2}) removal with C_0=30 mg/L and pH=5: Different dosages of CST-8,

The anti-interference ability of CST-8 was evaluated against K^+, Na^+, Fe^{3+}, Zn^{2+}, Cu^{2+}, Mg^{2+}, Al^{3+}, Ni^{2+}, Ca^{2+}, Cr^{3+}, SO_4^{2-}, Cl^-, and CO_3^{2-} (5:1 molar ratio vs (Mn^{+2})). As shown in Fig. 4, these ions have negligible impact on (Mn^{+2}) removal, demonstrating high tolerance. CST-8 also maintains 71 % removal efficiency after four cycles (Fig. 4). TEM of used CST-8 (Fig. 5) shows unchanged morphology and uniform U distribution, indicating partial adsorption without hindering recyclability [28].

XPS analysis reveals that (Mn^{+2}) is partially reduced to (Mn^{+2}) after photocatalysis (Fig. 4), confirming that photocatalytic reduction contributes to (Mn^{+2}) removal. Cd, Se, and Te remain in their original states (Fig. 4), with only a slight red shift for Se due to aerobic conditions. Te shows an increased Te^{4+} peak, suggesting oxidation of Te^{2-} during photocatalysis. Overall, the photo-induced reaction can be.

The active species responsible for (Mn^{+2}) photoreduction were investigated using various scavengers (Fig. 5). Under dark conditions, addition of h^+, ·OH, $\cdot O_2^-$, and e^- scavengers slightly increased (Mn^{+2}) removal. Upon light exposure, all scavengers reduced (Mn^{+2}) removal compared to the control, as reflected in their time-dependent rate constants. This indicates that h^+, ·OH, $\cdot O_2^-$, and e^- synergistically contribute to photocatalysis. Isopropanol (·OH) and 4-benzoquinone ($\cdot O_2^-$) yielded the highest rate constants (0.083 and 0.078 min^{-1}), highlighting them as primary active species, while $AgNO_3$ (e^-) showed a moderate effect (0.053 min^{-1}).[38], [39]. In contrast, EDTA-2Na and ammonium oxalate significantly suppressed (Mn^{+2}) reepresented stoichiometrically as $Te^{2-} + 3(Mn^{+2}) \rightarrow Te^{4+} + 3\ (Mn^{+2})$

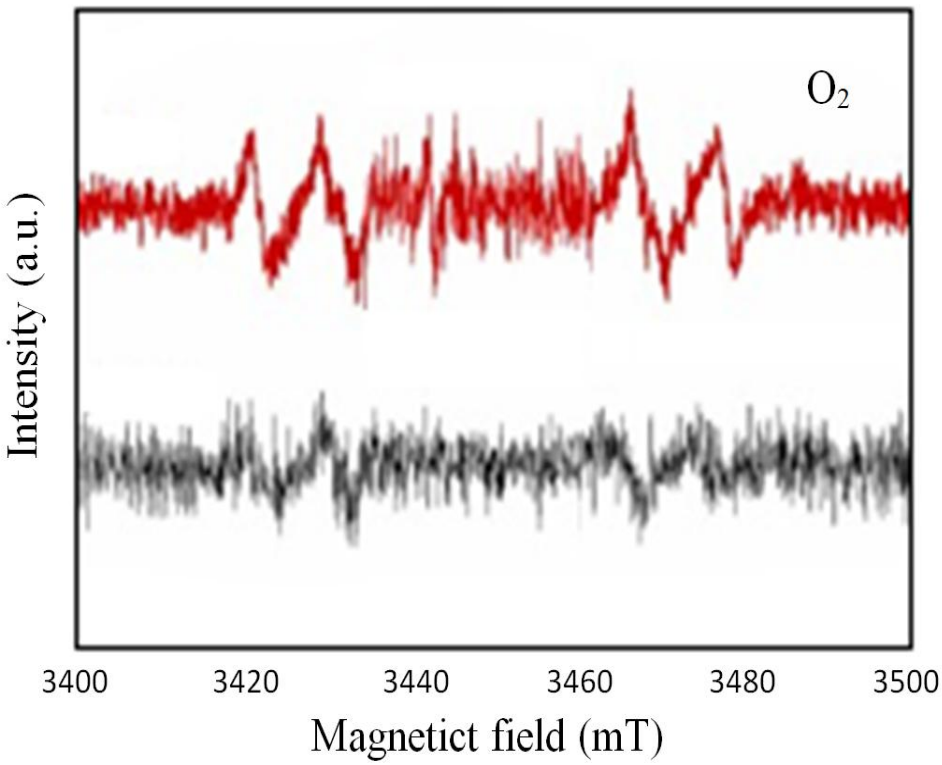

Fig. 5. The photocatalysis experiments with adding different sacrificial agents.

Overall, ·OH and $\cdot O_2^-$ are the primary active species driving photocatalysis. To confirm this mechanism, light-induced radicals on CST-8 were detected by EPR (Fig. 5), revealing characteristic signals of h^+, $\cdot O_2^-$, and ·OH. Here, h^+ initiates photoredox reactions, while $\cdot O_2^-$ and ·OH likely originate from water. The energy band structure of CST-8 was also studied. The optical band gaps (E_g) of CdSe and CdTe are 2.240 and 2.320 eV, respectively.Flat-band potentials (E_fb, vs Ag/AgCl, pH 7) are −1.308 eV for CdSe and −1.120 eV for CdTe [29], [40], .

The working mechanism of CST-8 for (Mn^{+2}) removal was further explored using photocurrent density (P_ph) to evaluate the transfer of photogenerated e^- and h^+ (0.5 M Na_2SO_4 as electrolyte). This optimization is attributed to the built-in electric field formed at the CdSe/CdTe heterojunction in CST-8, which enhances charge migration and Mn^{2+} photoreduction efficiencyt, thereby significantly improving the photoreduction of Mn^{2+}. A slight decrease of P_ph over time for CST-8, unlike the stable response of CdSe and CdTe, may result from irreversible oxidation of Te^{2-}, reducing heterojunction interfaces.

The proposed photocatalytic reactions are summarized as:

1. CST-8 + hv → e^-_CST-8 + h^+_CST-8
2. (Mn^{+2})+ 2 e^-_CST-8 → (Mn^{+2})
3. O_2 + e^-_CST-8 ↔ $\cdot O_2^-$
4. 2 $\cdot O_2^-$ + (Mn^{+2})→ (Mn^{+2}) + 2 O_2
5. 6 h^+_CST-8 + Te^{2-} → Te^{4+}
6. O_2 + 2 H_2O + 4 h^+_CST-8 ↔ 4 ·OH
7. 6 ·OH + Te^{2-} → Te^{4+}

Since the adsorption of (Mn^{+2}) on CST-8 under light is negligible (<0.1 %/min), (Mn^{+2}) reduction is attributed to electron-hole pairs generated by CST-8 upon irradiation .(Fig. 5). Light first enables CST-8 to produce e^- and h^+ (Eq. 1), and (Mn^{+2}) can be directly reduced by e^- to (Mn^{+2}) (Eq. 2). Additionally, photogenerated electrons react with dissolved O_2 to form $\cdot O_2^-$, which participates in the reduction of higher-valence manganese species to Mn^{2+}(Eq. 3, 4). Similarly, oxidative h^+ and ·OH can oxidize Te^{2+} to Te^{4+} (Eq. 5–7), with Eq. 5 and 7 suggesting that Te^{2-} may act as a dual sacrificial agent for both h^+ and ·OH. Based on these results, the stoichiometric photo-induced removal of (Mn^{+2}) can be summarized as:

Te^{2-} + 3 (Mn^{+2})→ Te^{4+} + 3 U(IV)

IV CONCLUSION

In this study, we report the successful design, synthesis, and comprehensive characterization of a novel CdSe/CdTe heterojunction, which exhibits outstanding performance in the photoreduction of Mn(IV) to Mn(II) under natural sunlight, completely eliminating the requirement for sacrificial agents. The prepared

heterojunction exhibits an outstanding (Mn^{+2}) removal efficiency of 92 % within a remarkably short time frame of only five minutes, accompanied by a high maximum removal rate of 14.4 mmol/(g·h), highlighting the potential of this system for rapid and practical uranium remediation applications.

These exceptional performances can be attributed to the deliberate interfacial and elemental engineering of the CdSe/CdTe heterostructure, which has been systematically validated through both experimental observations and theoretical calculations. The unique interfaces within the heterojunction are capable of generating an intrinsic electric field that not only promotes the efficient separation of photogenerated electron-hole pairs but also facilitates the rapid migration of electrons toward reactive sites, thereby minimizing recombination losses and maximizing photoreduction efficiency.

Furthermore, the presence of Te^{2-} within the heterostructure plays a crucial multifunctional role. It acts as a dual trap, scavenging both oxidative holes (h^+) and highly reactive ·OH radicals, which significantly enhances the overall photocatalytic process. This dual functionality, combined with the inherent adsorption properties of the heterojunction, creates a synergistic effect between adsorption and photocatalysis, leading to highly accelerated (Mn^{+2}) reduction.

The findings of this work not only advance our understanding of the fundamental photochemical behavior of CdSe/CdTe heterostructures but also demonstrate a viable strategy for developing highly efficient, sacrificial agent-free photocatalysts for uranium remediation. By providing both rapid kinetics and high removal efficiency, this heterojunction system holds great promise for practical applications in environmental remediation and nuclear wastewater treatment, and it may inspire future studies on the rational design of multifunctional photoactive materials for heavy metal removal under solar irradiation.

REFERENCES

[1]. Y. Bicer, I. Dincer.,[2017],Life cycle assessment of nuclear-based hydrogen and ammonia production options: a comparative evaluation.Int. J. Hydrog. Energ., 42 (33) p. 21564, 10.1016/j.ijhydene.2017.02.002

[2]. Z. Dai, Y. Zhen, Y. Sun, L. Li, D. Ding., [2021]$ZnFe_2O_4$/g-C_3N_4 S-scheme photocatalyst with enhanced adsorption and photocatalytic activity for uranium(VI) removal. Chem. Eng. J., 415 ,Article 129002, 10.1016/j.cej.2021.129002

[3]. Q. Xu, L. Zhang, J. Yu, S. Wageh, A.A. Al-Ghamdi, M. Jaroniec.,[2018]Direct Z-scheme photocatalysts: principles, synthesis, and applications.Mater. Today, 21 (10) p. 1054, 10.1016/j.mattod.2018.04.008

[4]. T. Chen, K. Yu, C. Dong, X. Yuan, X. Gong, J. Lian, X. Cao, M. Li, L. Zhou, B. Hu, *et al* [2022].Advanced photocatalysts for uranium extraction: elaborate design and future perspectives,Coord. Chem. Rev., 467 , 214615, 10.1016/j.ccr.2022.214615

[5]. X. Jiang, Q. Xing, X. Luo, F. Li, J. Zou, S. Liu, X. Li, X. Wang., [2018] Simultaneous photoreduction of Uranium(VI) and photooxidation of Arsenic(III) in aqueous solution over g-C_3N_4/TiO_2 heterostructured catalysts under simulated sunlight irradiation.Appl. Catal. B Environ., 228 , p. 33, 10.1016/j.apcatb.2018.01.062

[6]. D. Normile., [2021]Japan plans to release Fukushima's wastewater into the ocean.Science , 10.1126/science.abi9880

[7]. J. Zhang, D. Zhou, S. Dong, N. Ren. [2019] Respective construction of Type-II and direct Z-scheme heterostructure by selectively depositing CdS on {001} and {101} facets of TiO_2 nanosheet with CDots modification: a comprehensive comparison.J. Hazard. Mater., 366 , p. 317, 10.1016/j.jhazmat.2018.12.013

[8]. A. Kumar, M. Khan, J. He, I.M.C. Lo., [2020] Recent developments and challenges in practical application of visible-ight-driven TiO_2-based heterojunctions for PPCP degradation: a critical review..Water Res., 170 , Article 115356, 10.1016/j.watres.2019.115356

[9]. X. Yao, L. Chen, M. Liu, D. Feng, C. Wang, F. Lu, W. Wang, X. Wang, Y. Cheng, H. Liu, *et al.*., [2018]Rational design of Si/TiO_2 heterojunction photocatalysts: transfer matrix method.Appl. Catal. B Environ., 221 , p. 74, 10.1016/j.apcatb.2017.08.087

[10]. H. Bi, X. Yin, J. He, H. Song, S. Lu, Y. Ma, Z. Han. [2023], Conjugated organic component-functionalized hourglass-type phosphomolybdates for visible-light photocatalytic Cr(VI) reduction in wide pH range.Rare Met., 42 , p. 3646, 10.1007/s12598-023-02423-9

[11]. B. Wang, G.M. Biesold, M. Zhang, Z. Lin.,[2021]Amorphous inorganic semiconductors for the development of solar cell, photoelectrocatalytic and photocatalytic applications.Chem. Soc. Rev., 50 (12) , p. 6931, 10.1039/D0CS01134G

[12]. Y. Ye, J. Jin, F. Chen, D.D. Dionysiou, Y. Feng, B. Liang, H. Cheng, Z. Qin, X. Tang, H. Li, *et al.*, [2022]Removal and recovery of aqueous U(VI) by heterogeneous photocatalysis: Progress and challenges.Chem. Eng. J., 450 (3), Article 138317, 10.1016/j.cej.2022.138317

[13]. T. Chen, B. Liu, M. Li, L. Zhou, D. Lin, X. Ding, J. Lian, J. Li, R. He, T. Duan, *et al.*, [2021]Efficient uranium reduction of bacterial cellulose-MoS_2 heterojunction via the synergistically effect of Schottky junction and S-vacancies engineering.Chem. Eng. J., 406 , Article 126791, 10.1016/j.cej.2020.126791

[14]. W. Li, Q. Zhang, L. Dong, W. Zhang, L. Lin, Z. Chen., [2024] Selective photosynthesis of imines from biomass-derived aldehydes over Ni/TiO_2.Rare Met., 43 , p. 1121, 10.1007/s12598-023-02504-9

[15]. X. Gong, L. Tang, J. Zou, Z. Guo, Y. Li, J. Lei, H. Liu, M. Liu, L. Zhou, P. Huang, *et al.*[2022] Introduction of cation vacancies and iron doping into TiO_2 enabling efficient uranium photoreduction. J.Hazard.Mater., 423 (PtA), Article 126935, 10.1016/j.jhazmat.2021.126935

[16]. P. Duan, D. Lin, W. Yang, X. Huang, A. Sun, Q. Pan., [2022] Facile preparation of covalent organic frameworks@alginate composite beads for enhanced uranium(VI) adsorption.Rare Met., 41, p. 1327, 10.1007/s12598-021-01884-0

[17]. Z. Dai, J. Lian, Y. Sun, L. Li, H. Zhang, N. Hu, D. Ding., [2022] Fabrication of g-C_3N_4/Sn_3O_4/Ni electrode for highly efficient photoelectrocatalytic reduction of U(VI).Chem. Eng. J., 433 (3), Article 133766, 10.1016/j.cej.2021.133766

[18]. Y. Li, L. Shi, Y. Mao, Y. Zhang, H. Wang., [2022] Efficient reduction of uranyl under aerobic conditions by sodium and potassium Co-doped carbon nitride.Chem. Eng. J., 446 (1), Article 136872, 10.1016/j.cej.2022.136872

[19]. N. Liu, R. Li, J. Zhu, Q. Liu, R. Chen, J. Yu, Y. Li, H. Zhang, J. Wang., [2023] Z-scheme heterojunction ZnS/WO_3 composite: photocatalytic reduction of uranium and band gapregulationmechanism.J.ColloidInterf.Sci., 630 (PtB),p. 733, 10.1016/j.jcis.2022.10.151

[20]. S. Li, D. Pan, Z. Cui, Y. Xu, H. Shang, W. Hua, F. Wu, W. Wu., [2022] Synergistic effects of oxygen vacancies and heterostructures for visible-light-driven photoreduction of uranium.Sep. Purif. Technol., 301, Article 121966, 10.1016/j.seppur.2022.121966

[21]. Y. Guo, S. Li, F. Yang, C. Li, Y. Guo, K. Xuan, G. Wang, Y. Liu, J. Li., [2022] Efficient charge separation in sulfur doped $AgFeO_2$ photocatalyst for enhanced photocatalytic U(VI) reduction: the role of doping and mechanism insights.J. Hazard. Mater., 440, Article 129734, 10.1016/j.jhazmat.2022.129734

[22]. Z. Dong, Z. Zhang, T. Wang, D. Zeng, Z. Cheng, Y. Wang, X. Cao, Y. Wang, Y. Liu, X. Fan., [2022] Ingenious design of ternary hollow nanosphere with shell hierarchical tandem heterojunctions toward optimized Visible-light photocatalytic reduction of U(VI).Sep. Purif. Technol., 286 , Article 120418, 10.1016/j.seppur.2021.120418

[23]. Z. Li, Z. Zhang, Z. Dong, F. Yu, M. Ma, Y. Wang, Y. Wang, Y. Liu, J. Liu, X. Cao, *et al*[2022].Solar light-responsive CdS/UiO-66-NH_2 for ultrafast uranium reduction from uranium-containing mine wastewater without external sacrificial agents.Sep. Purif. Technol., 283, Article 120195, 10.1016/j.seppur.2021.120195

[24]. P. Liang, L. Yuan, K. Du, L. Wang, Z. Li, H. Deng, X. Wang, S. Luo, W. Shi., [2021]Photocatalytic reduction of uranium(VI) under visible light with 2D/1D Ti_3C_2/CdS.Chem. Eng. J., 420 (1), Article 129831, 10.1016/j.cej.2021.129831

[25]. Y. Zhang, S. Zhang, H. Sun, Z. Wang, F. Gao, J. Zhang, Z. Liu, M. Fang, X. Tan, X. Wang., [2022]Visible-light-driven photoextraction of uranyl by O-doped hexagonal-cubic CdSphaseheterojunction.JEnviron.Chem.Eng., 10 (6), 108781, 10.1016/j.jece.2022.108781

[26]. Y. Zhang, M. Zhu, S. Zhang, Y. Cai, Z. Lv, M. Fang, X. Tan, X. Wang., [2020]Highly efficient removal of U(VI) by the photoreduction of SnO_2/$CdCO_3$/CdS nanocomposite under visible light irradiation.Appl. Catal. B Environ., 279, 119390, 10.1016/j.apcatb.2020.119390

[27]. P. Li, J. Wang, Y. Wang, L. Dong, W. Wang, R. Geng, Z. Ding, D. Luo, D. Pan, J. Liang, *et al*., [2021] Ultrafast recovery of aqueous uranium: photocatalytic U(VI) reduction over CdS/g-C_3N_4.Chem. Eng. J., 425 , Article 131552, 10.1016/j.cej.2021.131552

[28]. C. Dong, T. Qiao, Y. Huang, X. Yuan, J. Lian, T. Duan, W. Zhu, R. He., [2021] Efficient photocatalytic extraction of uranium over ethylenediamine capped cadmium sulfide telluride nanobelts.ACS Appl. Mater. Interfaces, 13 (10) , p. 11972, 10.1021/acsami.0c22800

[29]. J. Wang, Y. Wang, W. Wang, Z. Ding, R. Geng, P. Li, D. Pan, J. Liang, H. Qin, Q. Fan[2020]Tunable mesoporous g-C_3N_4 nanosheets as a metal-free catalyst for enhanced visible-light-driven photocatalytic reduction of U(VI).Chem. Eng. J., 383 , Article 123193, 10.1016/j.cej.2019.123193

[30]. F. Gao, Z. Wang, M. Fang, X. Tan, S. Xu, M. Liu, G. Fei, L. Zhang.[2023] Interactions of uranium and thorium with arsenazo III in an aqueous medium.Nano Res., 16 (11) , p. 12777, 10.1007/s12274-023-6159-z

[31]. J. Li, W. Han, H. Liu, M. Su, D. Chen, G. Song., [2023]Simultaneous removal of Cs (I) and U (VI) by a novel magnetic AMP@ PDA@ Fe_3O_4 composite.J. Cleaner Prod., 409, p. 137140, 10.1016/j.jclepro.2023.137140

[32]. T. Chen, J. Zhang, H. Ge, M. Li, Y. Li, B. Liu, T. Duan, R. He, W. Zhu., [2020] Efficient extraction of uranium in organics-containing wastewater over g-C_3N_4/GO hybrid nanosheets with type-II band structure.J. Hazard. Mater., 384 , 121383, 10.1016/j.jhazmat.2019.121383

[33]. S. Li, J. Wang, Y. Xia, P. Li, Y. Wu, K. Yang, Y. Song, S. Jiang, T. Zhang, B. Li., [2021] Boosted electron-transfer by coupling Ag and Z-scheme heterostructures in CdSe-Ag-WO_3-Ag for excellent photocatalytic H_2 evolution with simultaneous degradation.Chem. Eng. J., 417, Article 129298, 10.1016/j.cej.2021.129298

[34]. Z. Wang, B. Li, H. Shang, X. Dong, L. Huang, Q. Qing, C. Xu, J. Chen, H. Liu, X. Wang, *et al*.., [2022] Photo-induced removal of uranium under air without external photocatalysts.Green. Chem., 24 (18), p. 7097, 10.1039/D2GC02739A

[35]. Y. Yu, W. Li, Y. Huang, H. Yang, X. Lv, H. Yan, D. Lin, S. Jiao, L. Hou, Z. Wu., [2024]Simultaneous efficient photocatalytic hydrogen evolution and degradation of dye wastewater without cocatalysts and sacrificial agents based on g-C_3N_5 and hybridized Ni-MOF derivative-CdS-DETA.Small , 2309577, 10.1002/smll.202309577

[36]. H. Wang, R. Hu, N. Wang, G. Hui, K. Wang, W. Xie, R. Cao.,[2021] Boosting photoanodic activity for water splitting in carbon dots aqueous solution without any traditionalsupportingelectrolyte.Appl.Catal.B.Environ., 296 ,Article 120378, 10.1016/j.apcatb.2021.120378

[37]. R. Wang, S. Zhang, J. Zhang, J. Wang, H. Bian, L. Jin, Y. Zhang., [2024] State-of-the-art of lignin-derived carbon nanodots: preparation, properties, and applications.Int. J. Biol. Macromol., 273 (Pt 2) (2024), Article 132897, 10.1016/j.ijbiomac.2024.132897

[38]. P. Makuła, M. Pacia, W. Macyk[2018].,How to correctly determine the band gap energy of modified semiconductor photocatalysts based on UV-Vis spectra.J. Phys. Chem. Lett., 9 (23) , p. 6816, 10.1021/acs.jpclett.8b02892

[39]. W. He, Q. Xiao, Z. Qiu, F. He, Q. Chen, L. Hu, H. Wang., [2024] Synergistic piezo-photocatalytic reduction of U(VI) by $Zn_{0.7}Cd_{0.3}S$ solid solution homojunction.Chem. Eng. J., 494 , Article 152947, 10.1016/j.cej.2024.152947